Korean J. Chem. Eng., 40(9), 2271-2281 (2023)
DOI: 10.1007/s11814-023-1414-2

pISSN: 0256-1115
eISSN: 1975-7220

Experimental study of cured dust layer structure parameters based on semantic segmentation

Bin Li, Zhongli Ji†, Junfeng Mu, Yulin Ren, and Zhen Liu

Beijing Key Laboratory of Process Fluid Filtration and Separation, College of Mechanical and Transportation Engineering, China University of Petroleum, Beijing

(*Received 8 November 2022 • Revised 28 February 2023 • Accepted 7 March 2023*)

Abstract−The structural properties of the dust layer, including its thickness, porosity, and particle size distribution, play a critical role in ensuring the high precision and long-term stability of filter elements. However, observing these properties is challenging due to the weak adherence and cohesiveness of the layer. To address this issue, atomization thermosetting glue was used to achieve pre-curing, and the entire dust layer was cured with epoxy resin. After the sample was frozen and fractured using liquid nitrogen, the boundaries of the dust particles became plainly visible. Traditional binarization techniques were insufficient in identifying the edges of the dust particles since the grayscale values of particles and their environment partially overlap. As a result, a deep learning model based on the DeeplabV3+ network architecture was used to identify particles in the dust layer and achieved an accuracy of 90.99%. The research reveals that pulse-jet cleaning can double the thickness of the local dust layer on adjacent filter elements. Additionally, the surface morphology of the filter element significantly impacts the shape and thickness of the dust layer, causing it to change dramatically. Uneven thickness of the dust layer can result in a higher number of dust particles passing through the filter element membrane.

Keywords: Filtration, Ceramic Filter, Dust Layer, Curing, Semantic Segmentation

INTRODUCTION

Surface filtration is a highly effective technology used for removing dust particles from dusty gas [1]. Ceramic filter elements are commonly used in industrial applications due to their low flow resistance, high structural strength, heat shock resistance, and chemical corrosion resistance. Dust particles are trapped on the surface of the filter element, forming a dust layer that can increase the pressure drop and energy consumption of the system. The dust layer must be periodically removed to achieve cyclic regeneration of the filter [2-4]. Reverse pulse-jet cleaning is a popular and successful method for filter element regeneration [5]. However, even after each pulse-jet cleaning, some dust particles may remain on the surface of the filter element, resulting in a residual dust layer. The presence of this layer can shorten the life cycle of the filter tube [6-8].

While the presence of a dust layer increases the pressure drop during filtration, it also enhances filtration efficiency. The thickness, porosity, and particle size distribution are key structural properties of the dust layer. The laser displacement measuring system can demonstrate the trend of the dust layer thickness over time, which is deposited layer by layer by particles. Once the accumulated thickness reaches a certain threshold, the dust layer undergoes compression and porosity reduction [9]. The compressibility of the dust layer is affected by the filter superficial velocity, particle size and size distribution, and particle shape [10,11]. The drag force on particles is proportional to the superficial velocity of filtration [12,13]. The particle equilibrium state is disturbed when the friction resistance between particles is insufficient to resist the drag force, and particles move to compress the dust layer, reducing its porosity and establishing a new force balance [14]. The porosity of the dust layer gradually decreases from the outside to the interior of the filter element due to the more significant extrusion of the innermost dust layer [15]. As porosity decreases, the permeability of the dust layer decreases, and the pressure drop across the filter element increases according to Darcy's law. A comparatively dense dust layer makes it more challenging for particles to detach, resulting in lower ash removal efficiency of the filter element [16,17].

As the temperature rises, the filtration condition deteriorates [18,19], and the filtration pressure drop is proportional to the gas viscosity [1]. The rate of residual pressure drop across the filter element increases with increasing temperature, while the cleaning efficiency of the ceramic filter decreases [16]. In addition, dust particles, such as biomass ash, can melt at high temperature, forming a low-melting compound that can create a liquid bridge force between the particles. This results in a significant drop in pulse-jet cleaning efficiency and can cause filter element failure [20-22].

Our laboratory utilized super glue to pre-cure offline samples that had undergone several filtration cycles, epoxy resin to embed and cure the pre-cured samples, and threshold segmentation image processing technology to process the sample cross section [23].

The cohesion and adhesion of the dust layer on the filter element are weak [24]. Even a tiny vibration during filter element disassembly might cause the dust layer structure to be destroyed. A few studies have been reported on the entire dust layer struc-

†To whom correspondence should be addressed.
E-mail: zhongliji117@yeah.net

tural characteristics of the ceramic filter element. In this work, to minimize damage to the dust layer structure throughout the experimental procedure, atomized thermosetting adhesive and epoxy resin were employed to perform online pre-curing and curing of the dust layer, respectively. Liquid nitrogen freezing technology was used to get a more complete particle boundary in the cross section of the dust layer.

Typically, threshold segmentation or adaptive threshold segmentation is utilized for particle boundary recognition [25,26]. For basic scenes with distinct grain boundaries, threshold segmentation has a high degree of efficacy and precision. However, threshold segmentation of particle detection in the dust layer appears to be infeasible because more particles share the same gray value as their surroundings and the boundary is unclear. With the advancement of computing hardware and algorithms, particularly the emergence of graphics processing units (GPU), a new machine learning approach known as "deep learning" has emerged. Deep learning is a subset of machine learning and, by extension, of the broader area of artificial intelligence [27]. In general, deep learning is distinguished by neural network topologies that include more hidden layers than their predecessors. As a result, deep learning can successfully simulate extremely complicated situations. The picture can be divided at the pixel level to accomplish the total identification of the image [28]. At the same time, the effect of location information and neighboring pixels is evaluated, which considerably increases the accuracy and efficiency of picture segmentation and classification. Furthermore, several current deep learning algorithms have been shown to beat human performance in a variety of picture categorization tasks [29]. A number of studies have used deep learning to segment several rock picture formats for petrophysical investigation, including sandstone SEM photos [30,31], micro-CT images [32,33], and reflected light microscopy images [34].

Therefore, a semantic segmentation algorithm based on deep learning is introduced to recognize and segment the dust particles in the dust layer at the pixel level. DeepLabV3+ has excellent training efficiency and segmentation accuracy compared with U-Net, FCN, Seg-Net, and PSP-Net [35,36]. In this research, DeepLabV3+ was utilized to process the dust layer image to investigate the changing laws of the dust layer structure.

MATERIALS AND METHODS

1. Particle & Filter Materials

The fly ash used in this study came from a thermal power plant in Pingdingshan, Henan Province, China. It was taken from the secondary electrostatic precipitator. Its median particle size d_{50} is 61.6 μm. The filter element was made of ceramic fiber, and the specification parameters are listed in Table 1.

Table 1. Properties for filter medium

Item	Parameter
Filter length (L, mm)	200
Inner diameter (D_{in}, mm)	40
Outer diameter (D_{out}, mm)	60
Material	Filter medium-SiC Filtration membrane-Mullite
Filtration membrane thickness (h, μm)	140-260
Air permeability (K, $\times 10^{-12}$ m^2)	3-5

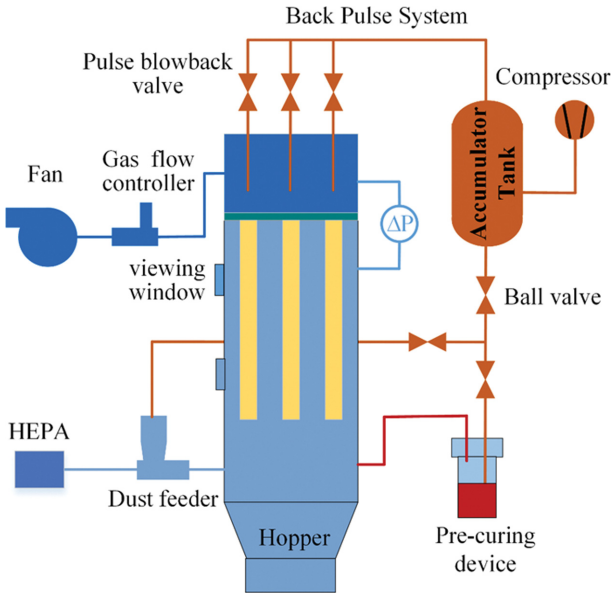

Fig. 1. Schematic diagram of the experimental system.

2. Experimental Condition

The experiment was carried out on the ceramic filter experimental system shown in Fig. 1. The filter chamber was cylindrical with a diameter of 240 mm and a length of 450 mm, and three ceramic filter elements were placed in the filter chamber. The experimental setup included a pulse back blowing valve (DMF-Z-20, 6 min inside diameter), a feeding machine (BEG-1000), a gas storage tank (100 L), a pulse controller (TBMM10, the pulse width of output is 35-350 ms), a differential pressure transmitter (PCM950S, range 0-1,000 Pa, accuracy 0.25% FS), and a gas mass flow controller (0-500 slpm, accuracy 0.6% FS).

The filtration system used a suction fan to create negative pressure downstream in order to generate gas flow. At the input, dust particles were injected to form dusty gas. The feeder controlled the concentration of dusty gas while the flow controller maintained the mass flow rate constant of filter gas.

The experimental conditions are shown in Table 2. The feeding

Table 2. Experimental conditions

Item	Parameter
Experimental temperature (T, °C)	25
Inlet dust concentration (g/m^3)	20
Superficial velocity (m/min)	1
Tank pressure (P_{t0}, MPa)	0.5
Pulse duration (Δt, ms)	100
Nozzle diameter (d, mm)	15
Jet distance (s, mm)	120
Cycle period (t, min)	30

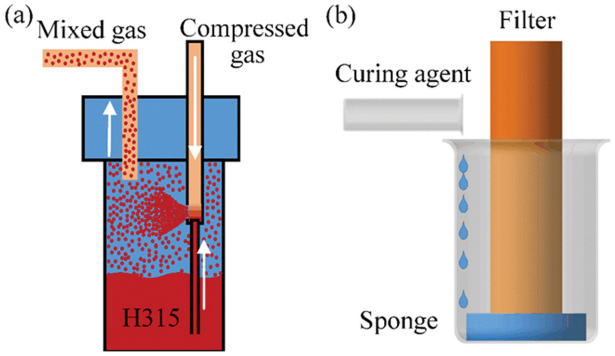

Fig. 2. Schematic diagram of dust layer curing. (a) Schematic diagram of the thermosetting adhesive atomizer, (b) Schematic diagram of epoxy resin wetting the dust layer under the capillary force.

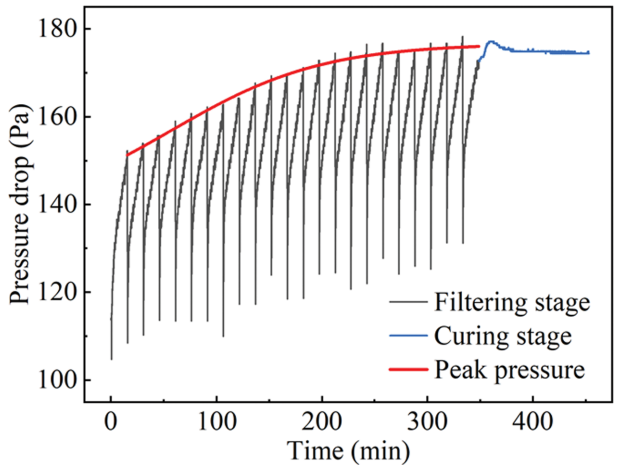

Fig. 3. Pressure drop across the filter element during the filtration and curing stages.

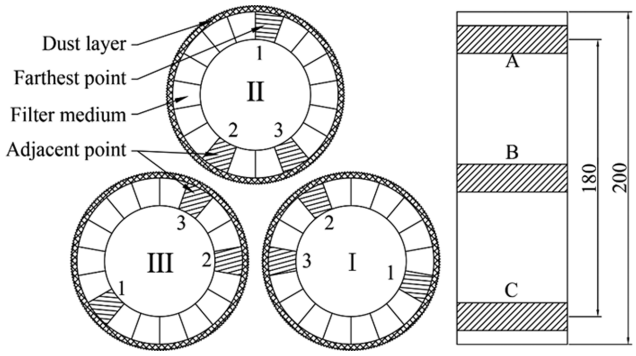

Fig. 4. Location diagram of sampling points.

is stopped with the fan to maintain working once the pressure drop across the filter element reaches a stable level to perform post-treatments such as pre-curing, curing, sample cutting, and freezing brittle fracture. For further information, see the next section.

3. Dust Layer Curing

Resin embedding is a typical sample preparation process in scanning electron microscopy (SEM) analysis. The idea is to infiltrate a low-viscosity resin embedding agent into the sample and fill every pore space before it cures. The original microstructure of the sample is preserved by the solidified embedding agent [23]. The dust layer should be pre-cured to enhance the adhesion and cohesion forces of the dust layer and prevent damage to the dust layer during the curing process.

When the structure of the dust layer on the surface of the filter element is relatively stable, which is when the pressure drop of the filter element tends to be steady, online pre-curing was commenced. The pre-curing glue was Quinson H315, a low viscosity thermosetting adhesive that does not cure below 80 °C and cures entirely in 15 minutes at 120 °C. Atomization equipment with an ejector nozzle was used to atomize the thermosetting glue. Fig. 2(a) depicts the atomization principle. The thermosetting glue atomizes under the injection of the nozzle, enters the filter chamber with the compressed air, and reaches the surface of the filter element under the suction of the fan. The dust layer adheres to the surface of the filter element, and the dust particles have a high wetting capacity. As a result, the dust layer absorbs the majority of the thermosetting glue and embeds it between the particles.

The filter chamber was heated to 120 °C and kept for 15 minutes after the thermosetting glue atomization had been maintained for 90 minutes to finish the pre-curing of the dust layer. The filter pressure drop across the filter element increased slightly during the pre-curing process, as shown in Fig. 3, indicating that the thermosetting glue had seeped into the dust layer, reducing the porosity of the dust layer marginally. And the increased amplitude accounts for around 9.2% of the total filter pressure drop across the filter element. It can be considered that the pre-curing technique has minimal influence on the structure of the dust layer.

Epoxy resin TB-3882, curing agent, and diluent were employed to cure the dust layer in a 2 : 1 : 7 ratio. Diluent was primarily used to lower epoxy resin viscosity and enhance permeability. The epoxy resin had high transparency and low shrinkage (2%) after curing. The embedding agent can be penetrated in two ways: one is to drip from top to bottom under the force of gravity, and the other is to infiltrate from bottom to top, utilizing the capillary force of porous media to reduce the number of air bubbles entrained by the embedding agent and improve the curing effect of the dust layer [23,37]. The bottom-up infiltration strategy was used in this research. The schematic diagram of the curing device is shown in Fig. 2(b). We put the ceramic filter tube into the beaker containing a sponge, then slowly poured the embedding agent into the beaker using a measuring cylinder. Under the influence of capillary force, the epoxy resin constantly seeps through the sponge into the filter tube and the dust layer.

We took three 1 cm high rings along the upper, middle, and bottom sections of the filter element axis after curing, and then three 1cm cubes on each ring (two nearest to the adjacent filter element and one near the wall of the filter chamber). A total of nine samples were obtained. Fig. 4 depicts the exact location and serial number of the samples.

There were two different types of treatment sample methods to observe the cross section of the dust layer: (a) alcohol was used to clean the sample after grinding and polishing it; (b) the brittle frac-

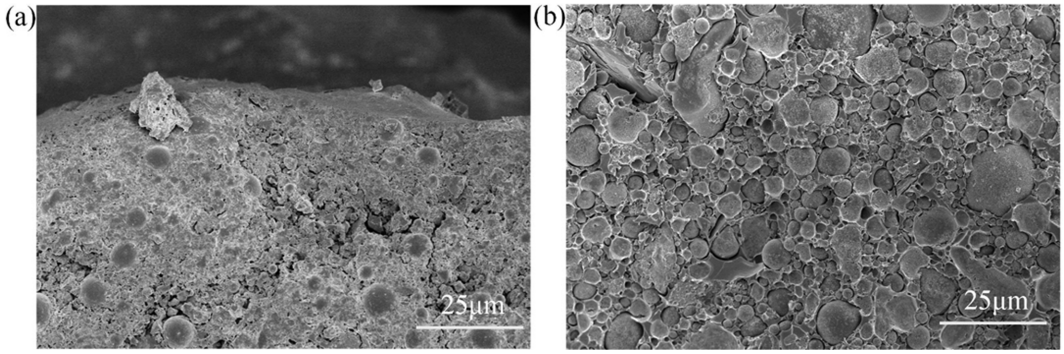

Fig. 5. Sectional view of the dust layer. (a) Sanding and polishing, (b) brittle fracture.

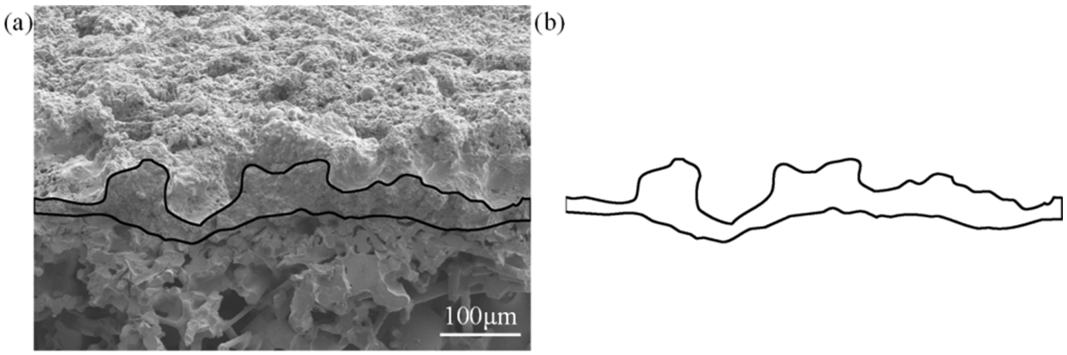

Fig. 6. Schematic diagram of dust layer contour extraction. (a) Labeling the contour of the dust layer, (b) dust layer profile after binarization.

ture was performed after the sample had been frozen using liquid nitrogen. Fig. 5(a) and 5(b) are sectional electron micrographs of the dust layer that were made by polishing, grinding, and freezing the brittle fracture with liquid nitrogen, respectively. The grinding and polishing of samples disrupted the shape of dust particles, making it impossible to distinguish between particles and epoxy resin. The morphology of the particles in the samples treated with liquid nitrogen freezing embrittlement, on the other hand, was plainly visible. Finally, it was decided to treat the sample with liquid nitrogen to freeze the brittle fracture.

Fig. 6(a) depicts the contours of the dust layer. The thickness of the dust layer is on the micron scale. Meanwhile, the contours of the dust layer fluctuated wildly, which made it difficult to quantitatively analyze the contours. The average thickness was used for analysis.

Image-Pro Plus was used to highlight the inner and outer boundaries of the dust layer (the inner contour of the dust layer was the contour of the outside surface of the filter element), and the image was binarized to highlight the inner and outer contours of the dust layer, as shown in Fig. 6(b).

To get the average thickness of the dust layer, the total area of the dust layer is divided by the length of the dust layer. Eq. (1) was used to calculate the average thickness (H_l) of the dust layer:

$$H_l = A_l / L_t \tag{1}$$

where A_l is the entire area of the dust layer, L_t is the length of the SEM photograph.

To investigate the porosity change trend of the dust layer along the thickness direction, five SEM observation points were uniformly positioned in the thickness direction, as shown in Fig. 7(a). The porosity of the dust layer could be calculated by dividing the total area of the particles by the area of the SEM photograph.

The area A_{pt} and the number N of dust particles in the white region in the image are counted, which indicates the total area and number of dust particles. Eq. (2) can be used to calculate the porosity of the dust layer.

$$\varepsilon_0 = \frac{A_t - A_{pt}}{A_t} \times 100\% \tag{2}$$

where A_t is the total area of the dust layer in SEM photograph.

The particle diameter in the dust layer was estimated using the equal projected area diameter d_H (Heywood diameter), which is defined as the diameter of the circular area equal to the particle projected area A_p. d_H can be calculated by Eq. (3). The particle size distribution in the dust layer is analyzed by counting the number of particles in different particle size sections.

$$d_H = (4A_p / \pi)^{1/2} \tag{3}$$

The dust layer images were collected under the Hitachi UHR FE-SEM SU8000 Series microscope at a magnification of 5000×. The images collected were 8-bit (256 grayscale), and the resolution of the image was 1280×960 pixels. Before deep learning training, the layers of all photographs were duplicated twice and transformed into RGB images. A total of 195 SEM pictures were collected. There were 117 images in the training set, 39 images in the validation set, and the rest of the images were for testing at a ratio

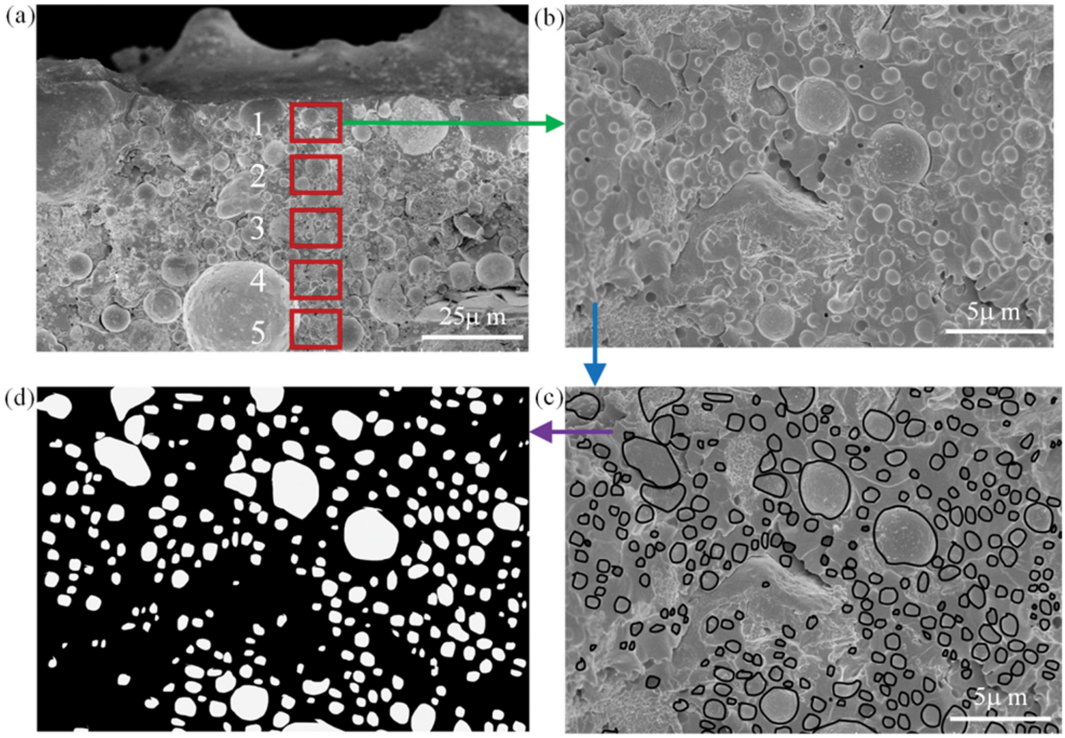

Fig. 7. Schematic diagram of SEM photograph particles labeling. (a) Schematic diagram of the observation point, (b) an SEM image of the observation point, (c) select the particle boundaries, (d) finished labeled image.

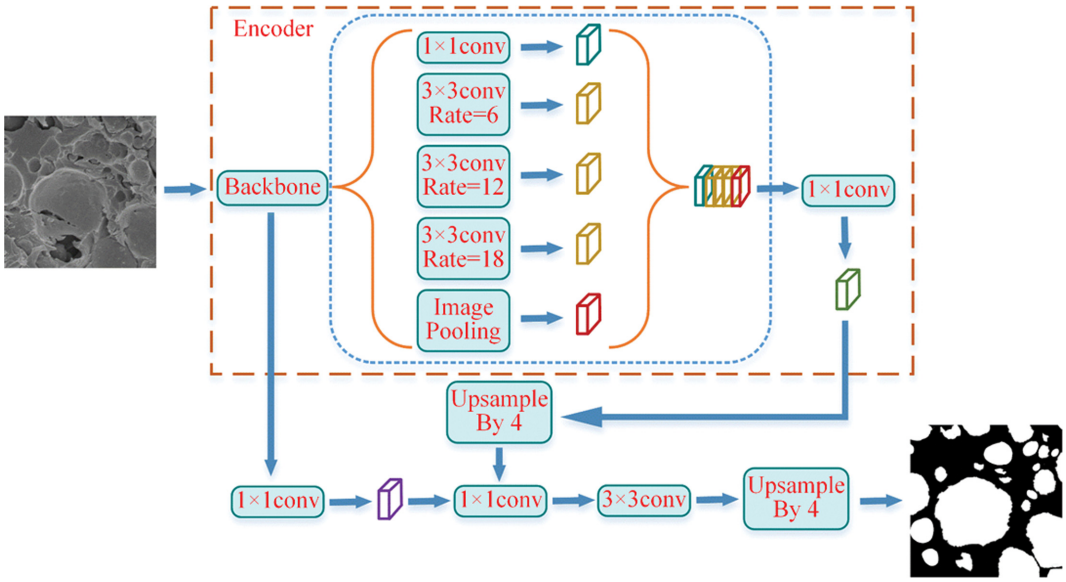

Fig. 8. Architecture of DeepLabv3+.

of 6 : 2 : 2.

4. Semantic Segmentation

After the experiment, the number II filter element was chosen at random for sample preparation and slicing for SEM observation. Fig. 7 shows a scanning electron microscope image of the dust layer generated by pre-curing, curing, slicing, freezing, and brittle fracture of the filter tube, in which the dust layer structure on the surface of the filter tube achieved a stable condition. The filter tube had undergone 23 filtering cycles at this point, as shown in Fig. 3. As illustrated in Fig. 7(b), most fly ash is spherical after high-temperature melting combustion. So, the particles were labeled based on the idea that they were round, with the exception of a few large particles that were non-spherical but could be easily labeled because they were distinct from the surroundings.

The SEM image was a frozen, brittle cross section of the dust layer, so the dust particles will appear randomly on the two cross

sections. When the dust particles are on the opposite side of the observation surface, a pit will inevitably form. When selecting particles, the pit was still considered to be dust particles.

The Lasso tool in Adobe Photoshop 2021 was used to build a selection border around the dust particles in the image. There were two types of image labels: particles (white) and epoxy resin (black), as shown in Fig. 7(c). Each image required an average of 2.5 hours to be labeled, which was a considerable amount of work.

Effective data enhancement can significantly enhance the semantic segmentation performance of the model and generalizability. In this work, translation, central rotation, and scaling were used as data enhancement techniques [38]. Since the number of particles was significantly more than that of epoxy resin, the data set was unbalanced, and there was a "long tail effect." Class weights were utilized for weighted balance in order to reduce its impact on training precision. To reduce overfitting, an L2 regularization penalty was applied to perform weight attenuation with an attenuation rate of 0.0002. As training data, the labelled images were incorporated into the semantic segmentation model. The optimal results were achieved by automatically training the model through iterative learning. Then, the test image was fed into the trained model to evaluate the effect of segmentation. Fig. 8 illustrates the network architecture of the DeepLabv3+ model proposed by Chen [39].

RESULTS AND DISCUSSION

1. Model Training Results

After 23 experimental cycles, the pressure drop and dust layer structure remained relatively stable. Subsequently, online pre-curing, curing, and liquid nitrogen freezing were carried out to minimize damage to the dust layer. Finally, electron microscopic observation was performed, and the image of the dust layer was subjected to semantic segmentation using the DeepLabv3+ model.

Fig. 9 shows the accuracy and loss function curves of the semantic segmentation model when it was being trained and validated. As per the graph, the model attained an accuracy of 91.25% and 90.99% during training and validation, respectively. Both the training and validation curves of the accuracy rate grow sharply at the outset and maintain a high level with minimal variation. The trends of the loss curves of the training set and the validation set are consistent, which shows that L2 regularization works well to fix the overfitting problem. From the comparison, it can be observed that the IOU value and accuracy of the validation set and the test set have a slight drop, but they have stay at a high level, as shown in Table 3. Randomly, an image was chosen to identify particles automatically, and then the results were compared to a picture that had been labeled by hand. Fig. 10 shows that the DeepLabV3+ deep

Table 3. Intersection over union (IoU), MeanBFScore and Pixel Accuracy values according to class

Classes	Parameters	Training set	Validation set	Test set
Particle	Accuracy	0.9129	0.9065	0.8991
	IoU	0.8774	0.8724	0.8671
	MeanBFScore	0.9901	0.9845	0.9856
Glue	Accuracy	0.9118	0.9015	0.8980
	IoU	0.8698	0.8664	0.8565
	MeanBFScore	0.9803	0.9763	0.9752

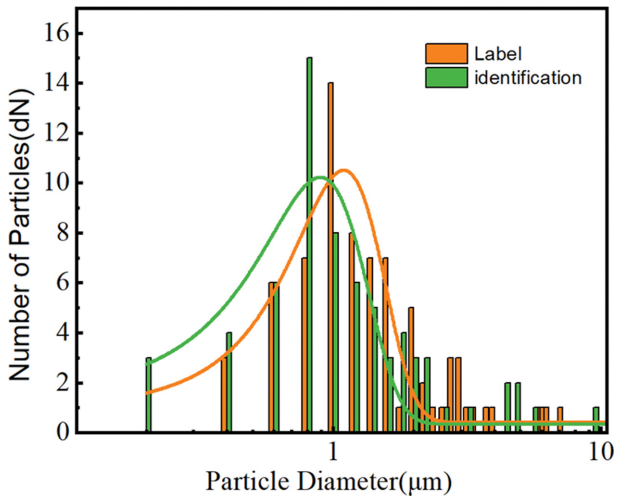

Fig. 10. Particle size distribution is obtained by different methods.

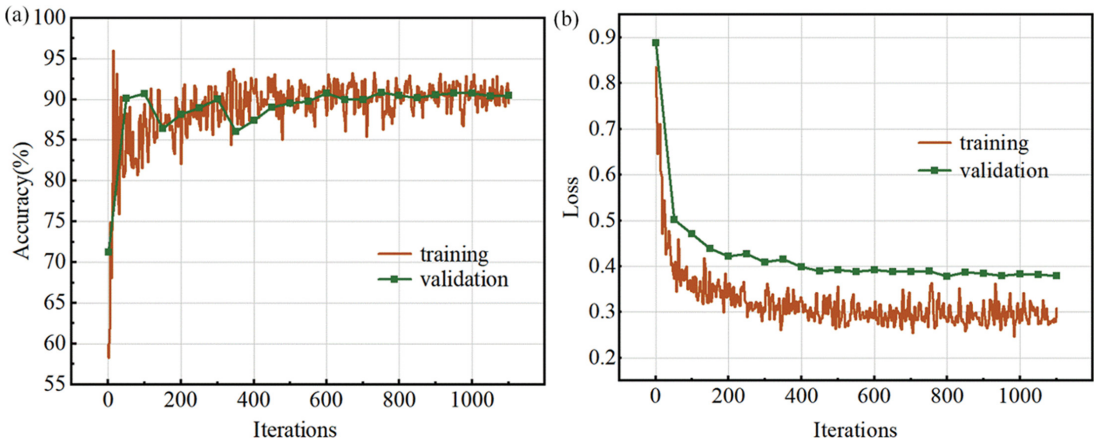

Fig. 9. Training curve of DL. (a) Loss curve during training process, (b) validation curve during training process.

learning network model can accurately identify particles in the dust layer and that the size distribution of the particles is consistent with the results that were marked by hand. However, there was a deviation of 0-2 μm between the particle size recognized by the model and the result of the calibration. There are two reasons for this: First, the width of the particle boundary is around 8-10 pixels wide. In the particle labelling procedure, the boundary will be designated as particles, which will increase the calibrated particle size. Second, the indistinct boundary between some particles and epoxy resin leads to identification errors. This difference is acceptable when compared to the significant time expense of manually labeling particles. Consequently, the DeepLabV3+ model could well be expanded to handle the particle identification problem in dust layers.

2. The Thickness of the Dust Layer

Table 4 shows the average thickness of the dust layer on the surface of the filter tube after 23 cycles. The dust layer thickness of sample No. 2 in each dust layer was larger than that of the other samples, respectively, for A, B, and C. In each row, the dust layer thickness of sample No. 2 is double that of sample No. 1. Meanwhile, sample No. 1 is the thinnest, and sample No. 3 is the second, and sample No. 2 is the thickest for each row of dust layers. The potential for the dust layer to bridge and filter element damage rises as the dust layer thickness increases. The primary reason for this phenomenon is the employment of three filter tubes in the experiment, each of which undergoes pulse-jet cleaning separately. When one filter element performs pulse-jet cleaning, the other two filter elements continue to filter normally. Under the influence of the air drag force, the dust particles that fall off the filter element during pulse-jet cleaning are reabsorbed on the surface of the normal filter element. This makes the dust layer on the surface of the normal filtration filter element thicker.

Table 4. The average dust layer thickness at the sampling points

The row of filter element	The column of filter element	Average thickness of dust layer (μm)
A	1	43.01
	2	96.58
	3	64.13
B	1	58.40
	2	96.94
	3	73.55
C	1	35.90
	2	76.47
	3	58.70

As seen in Fig. 4, the three filter elements were arranged in an equilateral triangle. The cleaning of filter tubes III and I has an impact on samples 2 and 3, respectively. There were three scenarios based on the pulse-jet cleaning sequence: (1) In each cycle, the number II filter element was the first to clean the dust, followed by the neighboring filter element. The thickness of the dust layer on samples No. 2 and No. 3 was similar in this case, and it was thicker

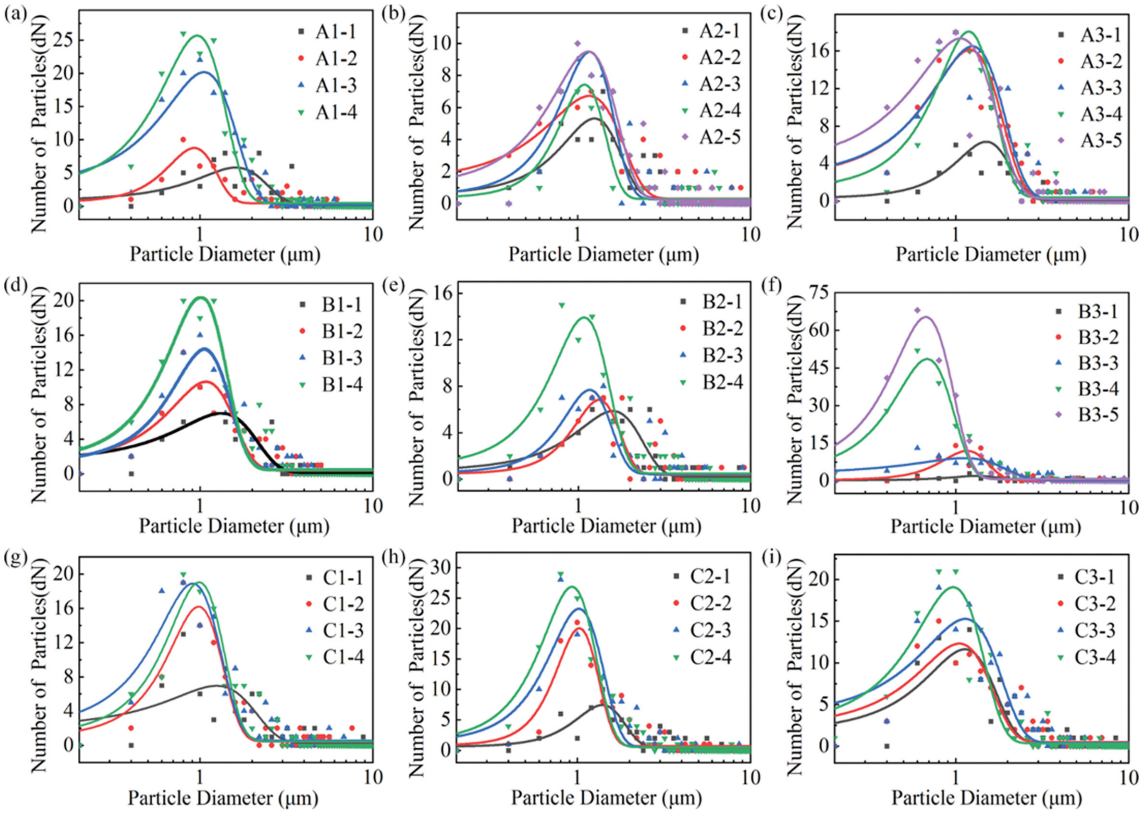

Fig. 11. The distribution of particle size at the sampling points.

than the thickness of the dust layer sample No. 1. This was because the cleaning of adjacent filter elements increased the thickness of the dust layer in samples 2 and 3 of the No. II filter element. Where sample No. 1 was less impacted since it was close to the wall of the filter room. (2) In each cycle, the number II filter element was cleaned for the second time, and there was one pulse-jet cleaning before and after the cleaning of number II filter element. The thickness of the dust layer in samples No. 2 and No. 3 significantly varied in this case. The pulse-jet cleaning of the No. II filter element eliminated the influence of the first cleaning filter tube. The Number II filter element was then influenced by the filter element that was pulse-jet cleaned at the end of the cycle. This resulted in a significant difference in the dust layer thickness between samples No. 2 and No. 3. (3) In each cycle, the Number II filter element was the last to undergo pulse-jet cleaning. The thickness of the dust layer between sample No. 1, sample No. 2, and sample No. 3 differs slightly in this case. The prior impact was weakened due to the pulse-jet cleaning of the Number II filter element.

The pulse-jet cleaning sequence of the filter element could be deduced from the thickness of the dust layer: I, II, and III. This matched the cleaning sequence used in the experiment. This indicates that pulse-jet cleaning has an impact on the surrounding filter tubes, especially those with unreasonable filter element spacing. Furthermore, this shows that the curing technique could be used to study the morphology of the dust layer.

3. The Distribution of Particle Size in the Dust Layer

Fig. 11 depicts the count distribution of particles of various particle sizes at nine observation locations in the upper, middle, and lower levels of the filter element. The particle size distribution within the observation point has a log-normal distribution. From the outside to the inside of the dust layer, the number of particles increased gradually, and the particle size decreased. The median particle size at each observation point was extracted to assess the changing trend of the particle size distribution in the thickness direction of the dust layer. Fig. 12 depicts the change in the median particle size in each row and column, which was used to evaluate the effect of pulse-jet cleaning on the dust layer of the filter element. Along with the thickness of the dust layer, the median particle size of the dust particles at the observation location decreased from the exterior to the interior. This is in accordance with previous results on the structure of two-dimensional filter cakes [40,41]. Meanwhile, Fig. 12 shows that there was no obvious rule for the median particle size of the dust layer in either the axial or circumferential directions of the filter tube. This is the result of two factors: First, to achieve dust solidification, the length of the filter tube was shortened to 200 millimeters. A shorter sampling interval tends to cause the samples at different sites to be similar. Second, because the dusty gas was spread uniformly in the filter tank, the dust layer that formed had an equal particle size distribution.

4. The Porosity of the Dust Layer

The porosity of the dust layer gradually reduced in the thickness direction as it got further away from the outer surface of the dust layer, as seen in Fig. 13. This was due to two factors: First, the drag force on dust particles gradually accumulates in the direction of gas motion. When the particle drag force exceeds the static friction between dust particles, the particles slide toward the inner side of the dust layer, causing compression and porosity reduction [42, 43]. Second, when filtration changes from reverse cleaning to forward filtration, a phenomenon called "backflow" happens in which the filtration speed is faster than the superficial gas velocity [44, 45]. The particles were re-adsorbed on the filter element by the backflow gas. Fine particles followed the backflow better and were more susceptible to it. The tiny particles reduce porosity by filling the pores in the dust layer. Similarly, there was no discernible regularity in the axial and circumferential porosities of the dust layer in the filter tube.

5. The Outline of the Dust Layer

The coordinate matrix of the inner and outer contours of the dust layer was extracted by finding the coordinates with the zero pixel value (black line) in the picture. Fig. 14 depicts the dust layer contours of nine sampling points. The distance between the inner and outer contours of the second column of the dust layer is greater

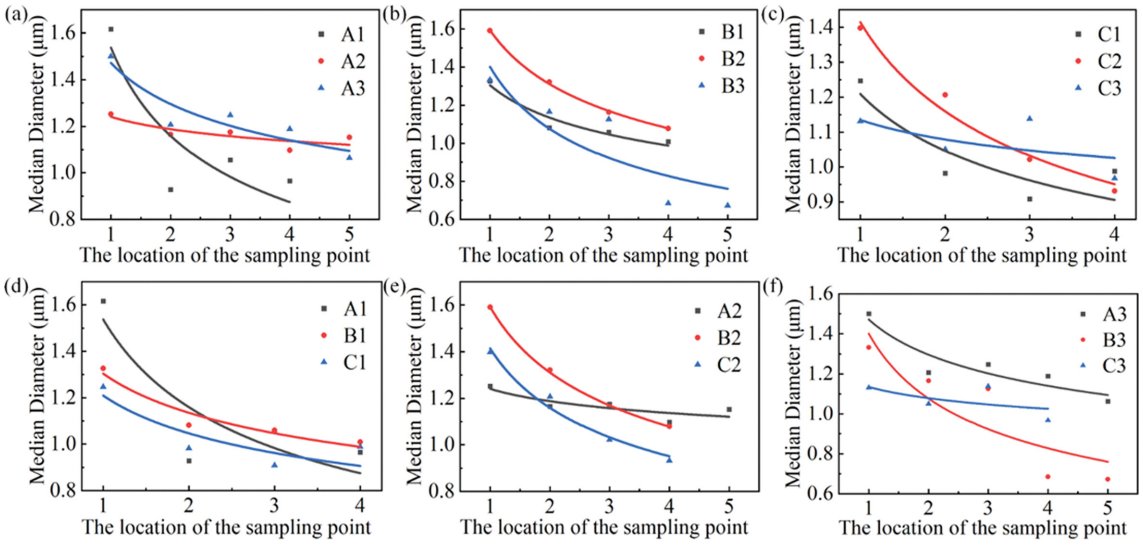

Fig. 12. Variation of the particle size distribution with the thickness of the dust layer.

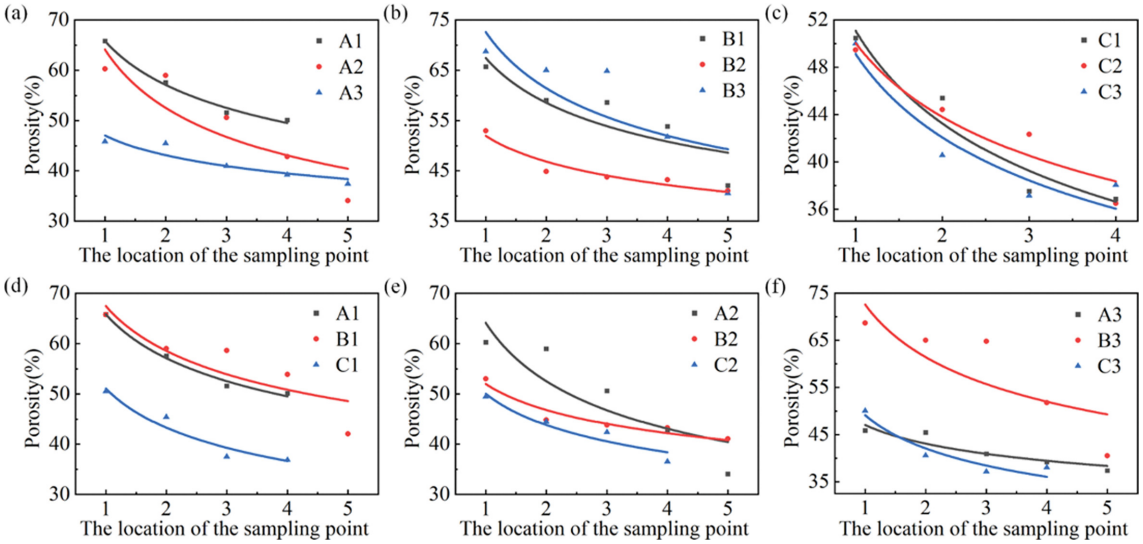

Fig. 13. Variation of the porosity of the dust layer with the thickness.

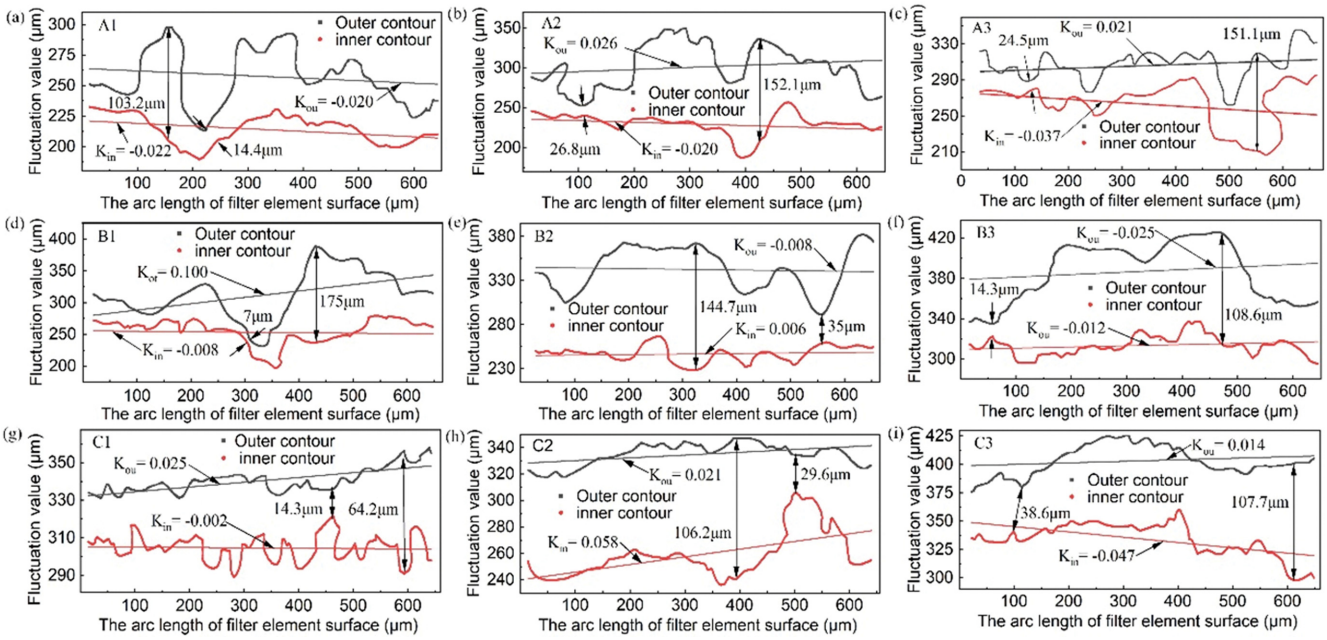

Fig. 14. The inner and outer contours of dust layer at nine sampling points.

than that of the first and third columns, which is consistent with the prior integrally determined average dust layer thickness.

The morphology of the dust layer was significantly influenced by the shape of the outer surface of the filter element. This agrees with earlier research on the effectiveness of different filter materials for filtration [46]. The micro-pores on the surface of the filter tube are essential for its high permeability. This small gap makes the surface of the filter tube uneven and has a significant effect on the capture and release of dust particles. The inner and outer contours of the filter element display a circular arc as a whole since the outside diameter of the filter element was 60 mm. The observation area of the SEM photograph was 630 μm long and 472.5 μm wide, which means the corresponding chord length is 630 μm, the corresponding radian is 0.021 rad, and the arch height is 1.7 μm. The arch height was much less than the fluctuation value (about 50 μm) of the inner and outer contours of the dust layer. As a result, a straight line could be used to fit the inner and outside features of the dust layer. The two straight lines after fitting were essentially parallel in Fig. 14, indicating that, despite the contour of the dust layer being quite random; it was consistent with the morphological features outside the filter element as a whole.

At the same time, Fig. 14(b), 14(e), 14(f) and 14(h) has a smaller included angle for the fitting line than other figures. It indicates that increasing the thickness of the dust layer weakened the influence of the outer surface morphology of the filter element on the contour of the dust layer and made the thickness of the dust layer

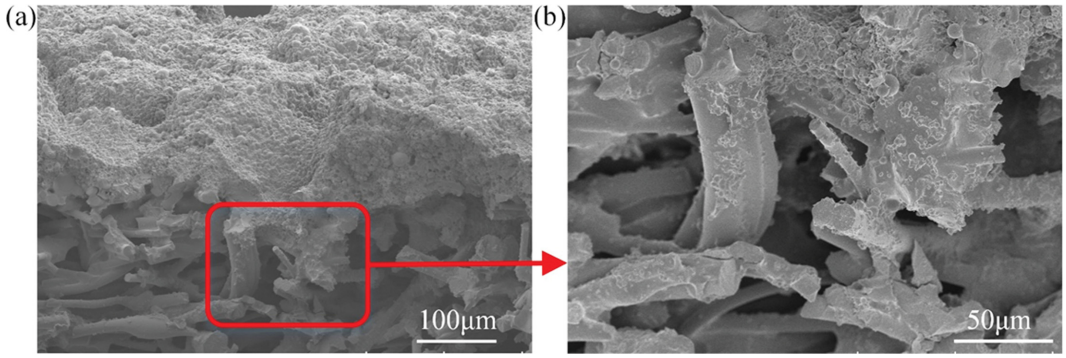

Fig. 15. Dust particles deposited in the filter medium.

more uniform. The thicker and more even dust layer makes it harder for particles to get through. This makes it easier for the filter tube to catch fine particles and further improves filtration efficiency [47].

The dust layer adheres to the exterior surface of the filter tube. As illustrated in Fig. 14, the outer contours of the dust layer are significantly affected by the uneven morphology of the outer surface of the filter element. The depression of the outer surface of the filter tube, in particular in Fig. 14(a), 14(b), 14(c), 14(d), and 14(f), will result in the depression of the dust layer contours. However, this influence is somewhat uncertain, as shown in Fig. 14(g) and 14(h), the fluctuations of the outer surface of the filter tube do not significantly alter the contours of the dust layer. This is because the microscopic morphology of the surrounding filter tube surface will influence the structural properties of the dust layer.

As the outside contour of the dust layer fluctuated up and down, the thickness of the dust layer changed dramatically. In addition, the thickness of the thinnest dust layer varied significantly across the region. The thinnest section of the dust layer in Fig. 14(c) is only 7 μm, one-eighth of the average thickness and one-twenty-fifth of the thickest segment.

Particles can easily penetrate the thin dust layer and deposit themselves in the filter element support. More tiny particles are lodged in the filter medium, as shown in Fig. 15. One of the primary reasons for the increased residual pressure drop across the filter element was the fine particles embedded [15,23].

CONCLUSION

We developed a method to perform on-line pre-curing of the dust layer using a thermosetting adhesive atomization device to prevent damage to the dust layer structure during subsequent experiments. The epoxy resin was then applied to the filter tube surface, utilizing capillary force to ensure complete curing of the dust layer. The samples were then treated with liquid nitrogen freezing and brittle fracture to fully display the particle boundaries in the cross section of the dust layer.

A semantic segmentation approach for dust particles in the dust layer was proposed based on the DeeplabV3+ deep learning model, which can more accurately distinguish particles and epoxy resin in SEM images. The validation set and test set showed high accuracy rates of 91.25% and 90.99%, respectively. Compared with the traditional binarization method, this approach achieved higher accuracy rates and significantly reduced the labor time required. This opens up new possibilities for SEM-image-based dust particle analysis systems.

The impact of pulse-jet gas on the adjacent filter element caused a significant increase in the thickness of the dust layer, with a higher risk of bridging as filtering time accumulated. The dust layer had a minimum thickness of only 7 μm, which was only one-eighth of its average thickness and one-twenty-fifth of its thickest point. The outer contours of the dust layer were significantly influenced by the surface morphology of the filter element. Moreover, the uneven thickness of the dust layer allowed more dust particles to pass through the filter element membrane and deposit in the filter medium, leading to increased pressure drop and reduced filtering efficiency.

ACKNOWLEDGEMENTS

The National Key Research and Development Program of China (2021YFB3801304) and the National Natural Science Foundation of China (No. 51904315) supported this work. The authors are also grateful to Prof. Haixia Li at Henan Polytechnic University for her suggestions and discussions.

DECLARATION OF COMPETING INTEREST

The authors declare that they have no known competing financial interests or personal relationships that could have appeared to influence the work reported in this paper.

REFERENCES

1. J. C. Lin, T. Hsiao, S. Hsiau, D. Chen, Y. Chen, S. Huang, C. Chen and M. Chang, *Sep. Purif. Technol.*, **198**, 146 (2018).
2. S. Berbner and T. Pilz, *Powder Technol.*, **86**, 103 (1996).
3. D. Koch, J. Seville and R. Clift, *Powder Technol.*, **86**, 21 (1996).
4. R. Boudhan, A. Joubert, S. Durécu, K. Gueraoui and L. Le Coq, *J. Aerosol Sci.*, **130**, 1 (2019).
5. L. F. Liu, *Korean J. Chem. Eng.*, **38**, 2122 (2021).
6. M. Lupion, B. Navarrete, B. Alonso-Farinas and M. Rodriguez-Galan, *Fuel*, **108**, 24 (2013).
7. K. Furumoto, T. Fukasawa, T. Ishigami, M. Irwan Fatkhur Rozy,

H.-P. Kuo, A.-N. Huang and K. Fukui, *Adv. Powder Technol.*, **33**, 103602 (2022).
8. J. H. Kim, Y. C. Kim and J. H. Choi, *Korean J. Chem. Eng.*, **33**, 726 (2016).
9. A. C. B. Neiva and L. Goldstein, *Chem. Eng. Process.*, **42**, 495 (2003).
10. J. H. Choi, S. J. Ha, Y. C. Bak and Y. O. Park, *Korean J. Chem. Eng.*, **19**, 1085 (2002).
11. D. Q. Jiang, W. D. Zhang, J. T. Liu, W. Geng and Z. Q. Ren, *Korean J. Chem. Eng.*, **25**, 744 (2008).
12. D. P. i. M. M. D. M. Kanaoka, T. Kishima and M. Furuuchi, *High Temperature Gas Cleaning* (1996).
13. C. R. N. Silva, V. S. Negrini, M. L. Aguiar and J. R. Coury, *Powder Technol.*, **101**, 165 (1999).
14. W. Höflinger, C. Stöcklmayer and A. Hackl, *Filtr. Sep.*, **31**, 807 (1994).
15. M. L. Aguiar and J. R. Coury, *Ind. Eng. Chem. Res.*, **35**, 3673 (1996).
16. J. H. Kim, Y. Liang, K. M. Sakong, J. H. Choi and Y. C. Bak, *Powder Technol.*, **181**, 67 (2008).
17. M. Hata, M. Furuuchi, C. Kanaoka, R. Kurose and H. Makino, *Adv. Powder Technol.*, **14**, 719 (2003).
18. A. Y. Al-Otoom, Y. Ninomiya, B. Moghtaderi and T. F. Wall, *Energy Fuels*, **17**, 316 (2003).
19. N. Döring, J. Meyer and G. Kasper, *Chem. Eng. Sci.*, **64**, 2483 (2009).
20. I. Tomasetta, D. Barletta and M. Poletto, *Adv. Powder Technol.*, **24**, 609 (2013).
21. L. G. Tong, X. D. Chen, Y. P. Zhang, S. W. Yin, C. P. Liu, L. Wang and Y. L. Ding, *Powder Technol.*, **354**, 760 (2019).
22. C. Kanaoka, M. Hata and H. Makino, *Powder Technol.*, **118**, 107 (2001).
23. H. Chi, Z. Ji and B. Du, *J. China Univ. Pet., Ed. Nat. Sci.*, **35** (2011).
24. P. C. Zhao and Y. G. Li, *Colloid Surf. A-Physicochem. Eng. Asp.*, **585** (2020).
25. S. Suresh and S. Lal, *Appl. Soft Comput.*, **55**, 503 (2017).
26. B. Li, W. Zhang, Y. Xue, R. Kong, W. Zhu, Y. Yu and Y. Chen, *Int. J. Rock Mech. Min. Sci.*, **158**, 105195 (2022).
27. L. Deng and D. Yu, *Found. Trends Signal Process.*, **7**, 197 (2014).
28. E. Shelhamer, J. Long and T. Darrell, *IEEE Trans. Pattern Anal. Mach. Intell.*, **39**, 640 (2017).
29. J. Stallkamp, M. Schlipsing, J. Salmen and C. Igel, *Neural Networks*, **32**, 323 (2012).
30. Y. Niu, P. Mostaghimi, M. Shabaninejad, P. Swietojanski and R. T. Armstrong, *Water Resour. Res.*, **56** (2020).
31. S. Karimpouli and P. Tahmasebi, *Comput. Geosci.*, **126**, 142 (2019).
32. P. I. Guntoro, G. Tiu, Y. Ghorbani, C. Lund and J. Rosenkranz, *Miner. Eng.*, **142**, 105882 (2019).
33. T. I. Anderson, B. Vega and A. R. Kovscek, *Comput. Geosci.*, **145**, 104593 (2020).
34. M. P. Filippo, O. da Fonseca Martins Gomes, G. A. O. P. da Costa and G. L. A. Mota, *Miner. Eng.*, **170**, 107007 (2021).
35. Y. Wang, X. Bai, L. Wu, Y. Zhang and S. Qu, *Fuel*, **308**, 121844 (2022).
36. T. A. Sipkens and S. N. Rogak, *J. Aerosol Sci.*, **152**, 105699 (2021).
37. H. Chi, Z. Ji and D. Sun, *J. China Univ. Pet., Ed. Nat. Sci.*, **23**, 72 (2010).
38. X. Tian and D. Hugh, *The Leading Edge*, **37**, 435 (2018).
39. L.-C. Chen, G. Papandreou, F. Schroff and H. Adam, *Rethinking atrous convolution for semantic image segmentation*, arXiv (2017).
40. E. Schmidt and F. Löffler, *Powder Technol.*, **60**, 173 (1990).
41. W.-M. Lu and K.-J. Hwang, *AIChE J.*, **41**, 143 (1995).
42. J. H. Choi, S. J. Ha and H. J. Jang, *Powder Technol.*, **140**, 106 (2004).
43. K. J. Jeon and Y. W. Jung, *Powder Technol.*, **141**, 1 (2004).
44. Z. Ji, S. Peng, H. Chen and M. Shi, *CIESC J.*, 35 (2003).
45. S. Peng, Z. Ji and H. Chen, *J. Combust. Sci. Technol.*, 498 (2002).
46. M. Saleem, G. Krammer and M. S. Tahir, *Powder Technol*, **228**, 100 (2012).
47. M. Koch and G. Krammer, *Powder Technol.*, **292**, 149 (2016).